LETTER

doi:10.1038/nature15510

CMT2D neuropathy is linked to the neomorphic binding activity of glycyl-tRNA synthetase

Weiwei He[1]*, Ge Bai[2]*, Huihao Zhou[1], Na Wei[1], Nicholas M. White[2], Janelle Lauer[3], Huaqing Liu[4], Yi Shi[1], Calin Dan Dumitru[1], Karen Lettieri[2], Veronica Shubayev[4], Albena Jordanova[5], Velina Guergueltcheva[6], Patrick R. Griffin[3], Robert W. Burgess[7], Samuel L. Pfaff[2] & Xiang-Lei Yang[1]

Selective neuronal loss is a hallmark of neurodegenerative diseases, which, counterintuitively, are often caused by mutations in widely expressed genes[1]. Charcot–Marie–Tooth (CMT) diseases are the most common hereditary peripheral neuropathies, for which there are no effective therapies[2,3]. A subtype of these diseases—CMT type 2D (CMT2D)—is caused by dominant mutations in *GARS*, encoding the ubiquitously expressed enzyme glycyl-transfer RNA (tRNA) synthetase (GlyRS). Despite the broad requirement of GlyRS for protein biosynthesis in all cells, mutations in this gene cause a selective degeneration of peripheral axons, leading to deficits in distal motor function[4]. How mutations in GlyRS (GlyRS^{CMT2D}) are linked to motor neuron vulnerability has remained elusive. Here we report that GlyRS^{CMT2D} acquires a neomorphic binding activity that directly antagonizes an essential signalling pathway for motor neuron survival. We find that CMT2D mutations alter the conformation of GlyRS, enabling GlyRS^{CMT2D} to bind the neuropilin 1 (Nrp1) receptor. This aberrant interaction competitively interferes with the binding of the cognate ligand vascular endothelial growth factor (VEGF) to Nrp1. Genetic reduction of Nrp1 in mice worsens CMT2D symptoms, whereas enhanced expression of VEGF improves motor function. These findings link the selective pathology of CMT2D to the neomorphic binding activity of GlyRS^{CMT2D} that antagonizes the VEGF–Nrp1 interaction, and indicate that the VEGF–Nrp1 signalling axis is an actionable target for treating CMT2D.

CMT diseases are a group of inherited disorders that specifically affect the peripheral nervous system and are characterized by progressive weakness and atrophy in the hands and feet[2,3]. Recent progress in neurogenetic studies has uncovered aminoacyl-tRNA synthetases as the largest gene family implicated in CMT. Among them, *GARS*, encoding GlyRS, was the first member identified, mutations in which cause a dominant axonal form of CMT (CMT2D)[4]. The canonical function of this evolutionarily ancient enzyme is to catalyse the ligation of glycine to the 3′ end of its cognate tRNA as the first step of protein synthesis. Interestingly, emerging evidence has revealed that GlyRS in multicellular organisms, like several other tRNA synthetase family members, has acquired the ability to be secreted from cells and as an extracellular protein can influence cell signalling[5–9].

More than a dozen missense *GARS* mutations (GlyRS^{CMT2D}) have been found in CMT2D patients, with varying degrees of genetic evidence for disease association[10–13]. Among them, three mutations (E71G, L129P and G240R) are the most tightly linked to the disease[11] (Fig. 1a). Spontaneous and *N*-ethyl-*N*-nitrosourea (ENU)-induced missense mutations in mouse *Gars* also cause CMT2D-like phenotypes[14,15] (Fig. 1a). These dominant mutations are found throughout the primary sequence of GlyRS, with some affecting the aminoacylation enzyme activity whereas others do not[11]. Mice with a heterozygous deletion of the *Gars* gene and a 50% reduction in glycyl-tRNA synthetase activity are normal[15]. Furthermore, overexpression of the wild-type GlyRS (GlyRS^{WT}) in a CMT2D-disease mouse fails to rescue the neuropathy[16]. These genetic experiments indicate that CMT2D may arise from an abnormal activity gained by GlyRS^{CMT2D} rather than a general defect in tRNA aminoacylation as initially suspected.

In common with most class II tRNA synthetases, GlyRS functions as a dimer for aminoacylation. Interestingly, despite being dispersed in three separate domains of GlyRS, all known CMT2D-causing mutations are located near the dimer interface in the GlyRS crystal structure[17]. We found that five different human mutations associated with CMT2D caused a conformational opening in GlyRS that exposes new protein surfaces to solution[17] (Fig. 1 b). To test if this conformational change also occurs in GlyRS^{CMT2D} linked to CMT-like phenotypes in mice, we performed hydrogen–deuterium exchange labelling on GlyRS(P234KY) and found that the mouse mutation likewise opens new surfaces of the GlyRS protein to solution (Fig. 1c and Extended Data Fig. 1). These findings suggest that the abnormal 'opening' is shared by many CMT2D mutants.

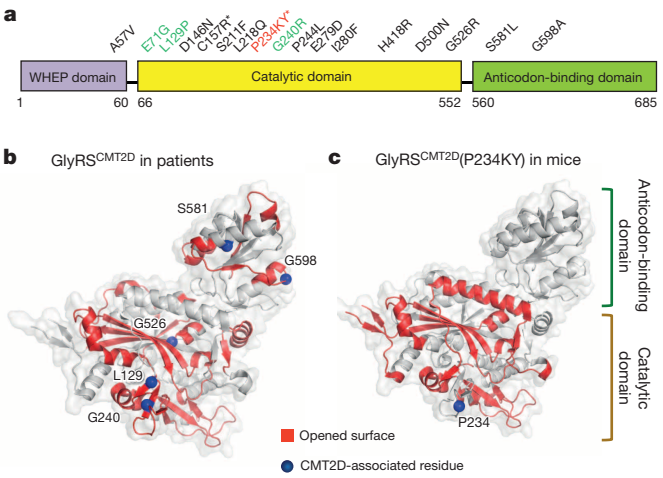

Figure 1 | Dispersed CMT2D mutations consistently cause neomorphic structural opening at the dimer interface of GlyRS. **a**, Distribution of 15 CMT2D-associated dominant mutations in the three domains of the cytosolic human GlyRS. The three strongest pathogenic mutations are highlighted in green. Two mutations identified in mice (asterisks) are labelled with their corresponding residue numbers in the human protein. **b**, Human GlyRS structure (monomeric subunit) viewed from dimer interface. Consensus opened-up areas caused by five CMT2D mutations are labelled in red[17]. **c**, Opened-up areas (red) by the P234KY mutation (>10% increase in deuterium incorporation relative to wild-type GlyRS).

[1]Departments of Chemical Physiology and Cell and Molecular Biology, The Scripps Research Institute, La Jolla, California 92037, USA. [2]Howard Hughes Medical Institute and Gene Expression Laboratory, The Salk Institute for Biological Studies, La Jolla, California 92037, USA. [3]Department of Molecular Therapeutics, The Scripps Research Institute, Jupiter, Florida 33458, USA. [4]Department of Anesthesiology, University of California San Diego, La Jolla, California 92093, USA. [5]Molecular Neurogenomics Group, VIB Department of Molecular Genetics, University of Antwerp, BE-2610 Antwerp, Belgium. [6]Department of Neurology, Medical University of Sofia, 1431 Sofia, Bulgaria. [7]The Jackson Laboratory, Bar Harbor, Maine 04609, USA.
*These authors contributed equally to this work.

©2015 Macmillan Publishers Limited. All rights reserved

The new surfaces exposed by mutations in GlyRS^{CMT2D} could lead to neomorphic protein interactions. This prompted us to search for binding partners unique to GlyRS^{CMT2D}. We performed a candidate-protein screen by *in vitro* protein pull-down assays. Because motor neurons are the most frequently affected neuronal type in CMT2D[4,18,19], our initial screen focused on molecules that are highly expressed by motor neurons and that have been linked to motor neuron diseases or defects. We detected strong binding between the receptor Nrp1 and several GlyRS^{CMT2D} mutants including P234KY and the three (E71G, L129P and G240R) with the strongest link to CMT2D in patients[11] (Fig. 2a and Extended Data Fig. 2a, b). In contrast, GlyRS^{WT} did not bind Nrp1 strongly, and GlyRS^{CMT2D} failed to bind to other motor neuron proteins such as TrkB (also known as Ntrk2), Dcc, Robo1 and Unc5C (Fig. 2a and Extended Data Fig. 2a, b). To confirm that this binding specificity occurs *in vivo*, we performed immunoprecipitations using neural tissues from wild-type and P234KY-mutated CMT2D mouse littermates. Anti-Nrp1 antibodies co-precipitated significantly more GlyRS from CMT2D mice than wild-type controls (Fig. 2b), indicating that GlyRS^{CMT2D}(P234KY) binds to Nrp1 *in vivo*. Furthermore, we also found that the GlyRS–NRP1 interaction is significantly stronger in CMT2D patients carrying the L129P mutation than in healthy individuals (Fig. 2c). To quantify these interactions, we used biolayer interferometry and a biosensor with immobilized Nrp1 on the surface. GlyRS^{WT} binding was undetectable at 1 μM, whereas GlyRS^{CMT2D} bound significantly more strongly, with a dissociation constant (K_d) of 29.8 ± 6.3 nM for L129P and 208.7 ± 53.8 nM for P234KY.

Next, we mapped the site where GlyRS^{CMT2D} binds to Nrp1 using pull-down assays with domain-deletion constructs. Removal of the extracellular a and c domains of Nrp1 did not alter GlyRS^{CMT2D} binding, whereas the extracellular Nrp1 b1 domain alone was sufficient to bind GlyRS^{CMT2D}(P234KY) (Fig. 2d and Extended Data Fig. 2c). Because the b1 domain is the binding site of VEGF-A$_{165}$, this finding raised the possibility that GlyRS^{CMT2D} might influence the binding of

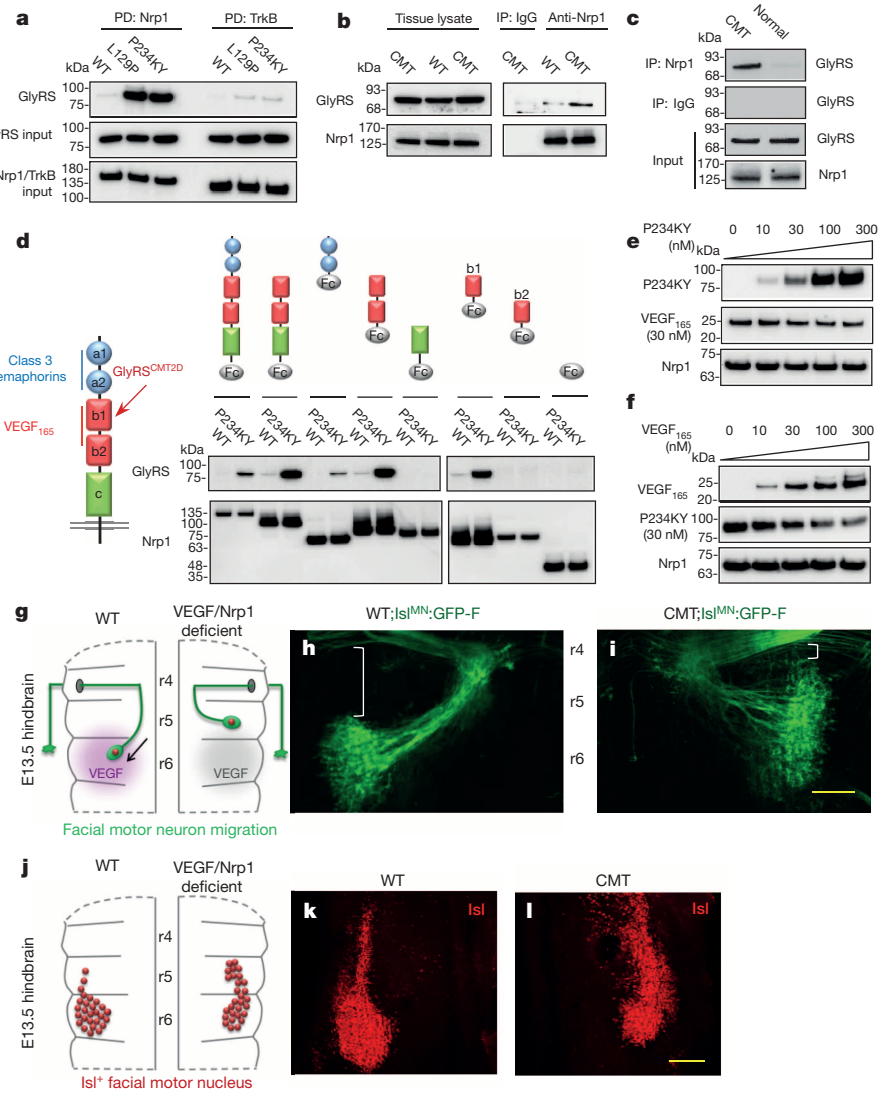

Figure 2 | GlyRS^{CMT2D} specifically binds Nrp1 and antagonizes VEGF–Nrp1 interaction. **a**, *In vitro* pull-down (PD) of GlyRS^{CMT2D} proteins by the ectodomain of Nrp1 but not TrkB. **b**, Co-immunoprecipitation (IP) to detect GlyRS–Nrp1 interaction in neural tissues of wild-type (WT) and P234KY-*Gars*^{CMT2D} mice (CMT). **c**, Co-immunoprecipitation to detect GlyRS–Nrp1 interaction in lymphocytes from CMT2D patients carrying the L129P mutation ($n = 5$) and from healthy individuals ($n = 3$). **d**, Domain mapping using *in vitro* pull-down identifies the b1 domain of Nrp1 as the main binding site of GlyRS^{CMT2D}. **e**, **f**, *In vitro* pull-down assay showing the competition between GlyRS^{CMT2D}(P234KY) and VEGF-A$_{165}$ proteins for Nrp1 (b domains) binding. **g**, **j**, Schematic of facial motor neuron migration (**g**) and facial motor nucleus (**j**) in open-book preparations of wild-type (left half) and VEGF–Nrp1-deficient mouse hindbrains at E13.5 (right half)[20]. **h**, **i**, Fluorescence labelling of facial motor neuron somata and axons by Isl^{MN}:GFP-F on one side of E13.5 mouse hindbrain of open-book preparation. **k**, **l**, Immunostaining of Isl-positive facial nucleus on one side of the E13.5 mouse hindbrain of open-book preparation. Scale bars, 200 μm.

©2015 Macmillan Publishers Limited. All rights reserved

VEGF-A_{165} to this region of Nrp1. Using pull-down assays, we found that increasing concentrations of P234KY or L129P $GlyRS^{CMT2D}$ compete with VEGF-A_{165} binding to the b domains of Nrp1 (Fig. 2e and Extended Data Fig. 2d). Conversely, increasing levels of VEGF-A_{165} displaced P234KY or L129P $GlyRS^{CMT2D}$ from the b domains (Fig. 2f and Extended Data Fig. 2e).

These observations led us to focus on GlyRS protein in the extracellular environment. Recent studies of $GlyRS^{WT}$ detected secretion from immune cells[8], so we first examined whether $GlyRS^{WT}$ is released by cell types relevant to the peripheral nervous system and motor function. Indeed, endogenous $GlyRS^{WT}$ was detected in the culture media of mouse motor neuron and differentiated myotube cell lines, but not of undifferentiated myoblasts (Extended Data Fig. 3a–e). We found that secreted $GlyRS^{WT}$ was enriched from extracellular sources using procedures that concentrate micro-vesicles (30–100 nm, 'exosomes') (Extended Data Fig. 4a, b). Extracellular levels of $GlyRS^{WT}$ were diminished by application of the exosome-pathway inhibitor GW4869 and enhanced by the exosome-pathway activator monensin (Extended Data Fig. 3a–f). Next, we checked whether CMT2D-causing mutations affect the secretion of $GlyRS^{CMT2D}$. Our results showed that $GlyRS^{CMT2D}$(P234KY) was detected at levels similar to $GlyRS^{WT}$ in the media of transfected cells (Extended Data Fig. 3g).

Nrp1 is a well-established receptor needed for motor neuron axon guidance and cell body migration[20,21]. Our finding that $GlyRS^{CMT2D}$ and VEGF-A_{165} compete for access to Nrp1 raised the possibility that CMT2D mice may phenocopy some features of VEGF-A_{164} (the mouse equivalent of human VEGF-A_{165}) and Nrp1 mutant mice[20]. VEGF–Nrp1 signalling is necessary for the caudal migration of facial motor neurons from rhombomere (r)4 to r6 during embryonic development (Fig. 2g, j)[20]. This provided us with an excellent *in vivo* assay to examine the effect of $GlyRS^{CMT2D}$ on a well-characterized system known to depend on VEGF–Nrp1 signalling. To track facial motor neuron migration we crossed CMT2D mice to transgenic Isl^{MN}:GFP-F reporter animals that selectively label facial motor neurons[22,23]. We found that CMT2D mutant embryos developed at a normal rate, appeared overtly normal based on their overall morphology, and that the expression levels of a variety of neuronal proteins were comparable to controls (Extended Data Fig. 5a, b). However, green fluorescent protein (GFP)-labelled facial motor neuron somata were found in ectopic anterior rhombomere locations in embryonic day (E)13.5 $GlyRS^{CMT2D}$ mutant embryos and manifested as an elongated stream across multiple rhombomeres (Fig. 2i). In contrast, most facial cells had completed their caudal migration to r6 in littermate controls at this stage (Fig. 2h). This observation was confirmed by immunostaining with the LIM homeodomain transcription factor Isl that is selectively expressed in the nuclei of facial branchiomotor neurons (Fig. 2k, l and Extended Data Fig. 5c). This facial motor neuron migration defect closely resembles the phenotypes of Nrp1-null and VEGF-A_{164}-null mice, as previously reported (Fig. 2j)[20]. Taken together, the protein-binding studies and embryological defects associated with $GlyRS^{CMT2D}$ suggested that $GlyRS^{CMT2D}$ inhibits VEGF–Nrp1 signalling.

VEGF signalling is thought to protect neurons from a variety of damaging insults[24]. Intriguingly, deficient VEGF signalling leads to the selective degeneration of motor neurons in mice[25]. To examine whether the VEGF–Nrp1 pathway is involved in motor deficits that arise from GlyRS mutations, we tested whether a genetic interaction could be detected between $Gars^{CMT2D}$ and *Nrp1*. Although the data described earlier suggest that $GlyRS^{CMT2D}$ attenuates normal Nrp1 signalling, it is still possible that $GlyRS^{CMT2D}$ might activate aberrant signalling through Nrp1 and cause motor defects. In the first case motor phenotypes should get more severe as *Nrp1* gene dosage is reduced in CMT2D mice, and in the second case motor phenotypes should improve. To test these possibilities, we intercrossed $Gars^{CMT2D}$ mice with *Nrp1* heterozygous ($Nrp1^{+/-}$) animals and characterized the motor behaviour of the single- and double-mutant offspring. At 2 weeks, when motor behavioural changes were not observed in either $Gars^{CMT2D}$ or $Nrp1^{+/-}$ mutant mice, 20% of the compound heterozygous $Gars^{CMT2D}/Nrp1^{+/-}$ mutant mice had developed neuromuscular dysfunction based on a hindlimb extension test (Extended Data Fig. 6a, b). At 4 weeks, CMT2D-like symptoms, including overt neuromuscular dysfunction and an altered walking stride, become apparent in $Gars^{CMT2D}$ mutants, whereas $Nrp1^{+/-}$ mice appeared normal (Fig. 3a–d and Supplementary Videos 1, 2). Strikingly, by 4 weeks, 50% of the $Gars^{CMT2D}/Nrp1^{+/-}$ mutant mice had entirely lost the ability to spread their legs and toes (Fig. 3a, b), and exhibited severely abnormal gait patterns (Fig. 3c, d and Supplementary Video 3). After postnatal week 4, $Gars^{CMT2D}/Nrp1^{+/-}$ mutant mice began to die. Consistent with our biochemical studies showing that $GlyRS^{CMT2D}$ binds poorly to other signalling receptors (see Fig. 2a and Extended Data Fig. 2a), intercrosses between $Gars^{CMT2D}$ and $TrkB^{+/-}$, $Dcc^{+/-}$, $Robo1^{+/-}$ and $Unc5C^{+/-}$ heterozygous mice did not worsen the neuromuscular

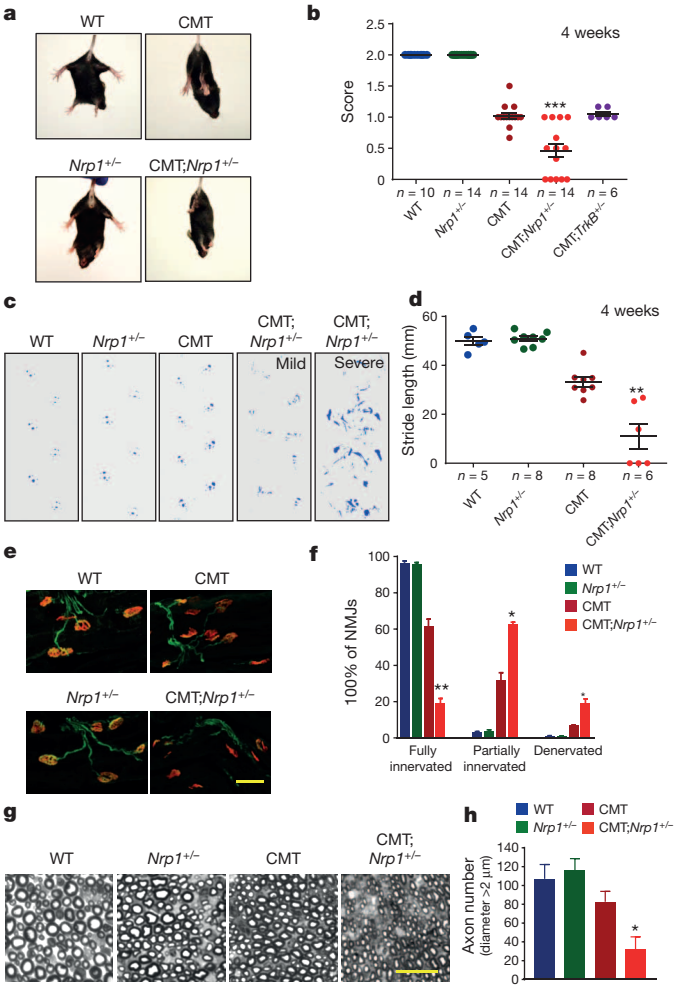

Figure 3 | *Nrp1* is a genetic modifier of CMT2D. **a**, **b**, Hindlimb extension test at 4 weeks. ***$P < 0.001$ (Mann–Whitney test). CMT, P234KY-$Gars^{CMT2D}$ mice. **c**, Hindlimb footprints of wild-type and mutant animals at 4 weeks. $Gars^{CMT2D}/Nrp1^{+/-}$ mutant mice exhibit disrupted gait patterns of different degrees (mild, severe). Note that severe cases show inability to walk. **d**, Stride length of wild-type and mutant animals at 4 weeks. **e**, **f**, Neuromuscular junctions immunostaining (NMJ) in the gastrocnemius muscles of 4-week-old mice with the motor nerve terminal labelled in green and acetylcholine receptors on the muscle labelled in red. Data are presented as mean values ± standard error of the mean (s.e.m.). $n = 3$ mice per group. Scale bar, 50 µm. **g**, **h**, Myelinated axons from sciatic nerves of 4-week-old mice. Scale bar, 20 µm. **h**, Histogram showing the quantification of axon numbers with the diameter larger than 2 µm. $n = 3$ mice per group. **d**, **f**, **h**, *$P < 0.05$, **$P < 0.01$ (*t*-test).

©2015 Macmillan Publishers Limited. All rights reserved

phenotypes in the compound heterozygotes (Fig. 3b and Extended Data Fig. 6c).

The motor defects in *Gars*^{CMT2D} and *Gars*^{CMT2D}/*Nrp1*$^{+/-}$ mutants were accompanied by marked pathological changes in the peripheral nerves and synaptic contacts with muscle fibres. Neuromuscular junctions (NMJs) displayed a normal apposition of nerve fibres and postsynaptic acetylcholine receptors in wild-type and *Nrp1*$^{+/-}$ animals, while partially innervated and completely denervated NMJs were present in 4-week *Gars*^{CMT2D} mutants (Fig. 3e, f). The loss of nerve terminals at NMJs was markedly increased in *Gars*^{CMT2D}/*Nrp1*$^{+/-}$ mutants (Fig. 3e, f). Likewise, at 4 weeks of age many large-diameter axons were absent from the sciatic nerves of *Gars*^{CMT2D} mutants compared with wild-type and *Nrp1*$^{+/-}$ littermates (Fig. 3g, h and Extended Data Fig. 7a–c). The absence of large-diameter axons was even more dramatic in 4-week *Gars*^{CMT2D}/*Nrp1*$^{+/-}$ compound mutants, and was comparable to the extreme axonal dystrophy observed in late-stage CMT2D mutants (Fig. 3g, h and Extended Data Fig. 7d)[15]. These findings demonstrate that *Nrp1* is an important genetic modifier of CMT2D pathology and that GlyRS^{CMT2D} antagonizes normal Nrp1 signalling rather than activating aberrant signalling.

These findings prompted us to test whether VEGF overexpression could counteract GlyRS^{CMT2D} and help to slow the loss of motor function in CMT2D mice. A lentiviral vector encoding either VEGF-A_{165} or GFP was injected bilaterally into the hindlimb muscles of *Gars*^{CMT2D} mutant mice at postnatal day 5, before the onset of overt motor defects (Fig. 4a and Extended Data Fig. 8). By 4 weeks of age, we began to observe a reduction of limb strength in the control GFP-treated *Gars*^{CMT2D} animals using an inclined plane test (Fig. 4b). However, VEGF-A_{165}-treated animals retained greater neuromuscular capacity with significantly higher scores (Fig. 4b). By 7 weeks, *Gars*^{CMT2D} animals exhibited a disrupted gait pattern with shortened hindlimb stride length, while VEGF-A_{165}-treated animals maintained a significantly longer walking stride (Fig. 4c). Likewise, VEGF treatment significantly improved the motor performance of *Gars*^{CMT2D} mutants in the rotarod test (Fig. 4d). To minimize the possible influence from the natural variation in disease progression among individual animals, we compared the effect of VEGF treatment to GFP controls by separately treating each hindlimb from the same animal.

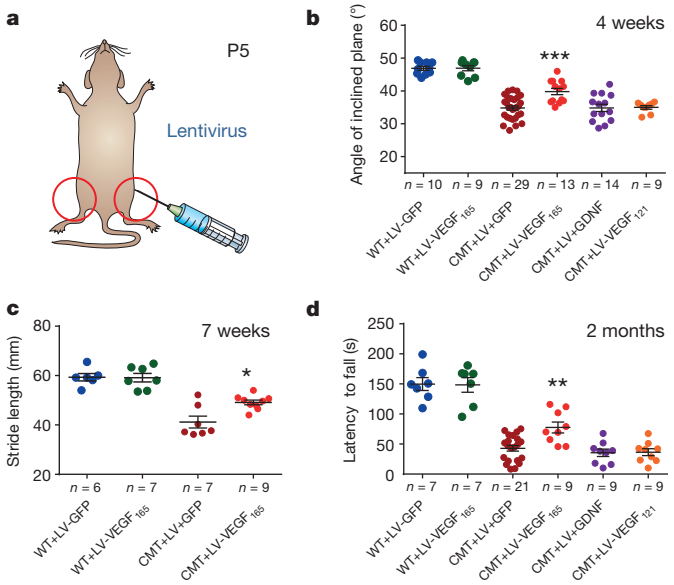

Figure 4 | VEGF treatment improves motor function in CMT2D mice. **a**, Diagram showing bilateral intramuscular injection of lentivirus (LV) into mouse hindlimbs at postnatal day (P)5. **b**, Inclined plane test of 4-week-old animals. **c**, Walking strides of 7-week-old animals. **d**, Rotarod test of 2-month-old animals. $*P < 0.05$, $**P < 0.01$, $***P < 0.001$ (*t*-test).

Lentiviral vectors encoding VEGF-A_{165} or GFP were injected unilaterally into each hindlimb of the same *Gars*^{CMT2D} mutant mouse at postnatal day 5 (Extended Data Fig. 9a). At 5 weeks, GFP-treated hindlimbs developed severe muscle weakness, largely losing their ability to extend. In contrast, the contralateral hindlimbs treated with VEGF-A_{165} retained significant function (Extended Data Fig. 9b–e). These results suggest that VEGF treatment significantly ameliorates the loss of motor function in CMT2D mice.

A number of neurotropic factors have been tested as broad-spectrum strategies to enhance neuronal survival and treat motor diseases[26–30]. This raised the possibility that VEGF might slow the progression of CMT2D pathology by functioning as a generic trophic factor rather than as a specific agent to restore normal VEGF–Nrp1 signalling. Therefore, we tested the effects of lentivirus-mediated expression of GDNF, a potent neurotrophin that has been used to enhance motor function and survival in mouse models of amyotrophic lateral sclerosis[26,27]. Unlike VEGF-A_{165}, we found that GDNF failed to slow disease progression in *Gars*^{CMT2D} mice (Fig. 4b, d and Extended Data Fig. 9f). Next, we tested whether VEGF-mediated motor sparing is dependent upon Nrp1 binding, by exploiting the binding specificity of VEGF protein isoforms. VEGF-A_{121} has overlapping functions with VEGF-A_{165} but lacks high-affinity Nrp1 binding[24]. We found that VEGF-A_{121} treatment failed to ameliorate the loss of motor function in CMT2D animals (Fig. 4b, d and Extended Data Fig. 9g). These data support a model in which VEGF treatment helps to guard against the motor loss arising from the aberrant activity of GlyRS^{CMT2D} by restoring VEGF–Nrp1 signalling.

Our results identify the *Nrp1* gene as an important genetic modifier for CMT2D, and link the selective pathology of this disease to the neomorphic binding of GlyRS^{CMT2D} to the receptor Nrp1. Although we found the same neomorphic binding to NRP1 in several human GlyRS^{CMT2D} mutants that are strongly disease associative (Fig. 2a and Extended Data Fig. 2a, b), we cannot rule out the possibility that some GlyRS^{CMT2D} mutants may interact with other extracellular and/or intracellular targets. Nevertheless, our findings strongly suggest that the VEGF–NRP1 pathway is an actionable target for treating CMT2D (Extended Data Fig. 10). While the exact role of VEGF in the motor system remains poorly defined, VEGF-deficient mice selectively develop symptoms of motor neuron disease over time[25]. The direct antagonism of VEGF–Nrp1 signalling by GlyRS^{CMT2D} found here further indicates that deficient VEGF signalling may represent a common pathogenic pathway that is susceptible to abnormal activity in other motor neuron diseases. A broad implication from this work is that the molecular basis of selective neuronal vulnerability in neurodegenerative diseases may arise from the neomorphic activity of misfolded proteins interacting with susceptible signalling targets in specific cell types. This conceptual framework may be applied for identifying additional druggable targets to treat neurodegenerative diseases, including other forms of CMT.

Online Content Methods, along with any additional Extended Data display items and Source Data, are available in the online version of the paper; references unique to these sections appear only in the online paper.

Received 7 August 2014; accepted 21 August 2015.
Published online 21 October 2015.

1. Saxena, S. & Caroni, P. Selective neuronal vulnerability in neurodegenerative diseases: from stressor thresholds to degeneration. *Neuron* **71,** 35–48 (2011).
2. Skre, H. Genetic and clinical aspects of Charcot-Marie-Tooth's disease. *Clin. Genet.* **6,** 98–118 (1974).
3. Patzkó, A. & Shy, M. E. Update on Charcot-Marie-Tooth disease. *Curr. Neurol. Neurosci. Rep.* **11,** 78–88 (2011).
4. Antonellis, A. *et al.* Glycyl tRNA synthetase mutations in Charcot-Marie-Tooth disease type 2D and distal spinal muscular atrophy type V. *Am. J. Hum. Genet.* **72,** 1293–1299 (2003).
5. Wakasugi, K. & Schimmel, P. Two distinct cytokines released from a human aminoacyl-tRNA synthetase. *Science* **284,** 147–151 (1999).
6. Yao, P. & Fox, P. L. Aminoacyl-tRNA synthetases in medicine and disease. *EMBO Mol. Med.* **5,** 332–343 (2013).

©2015 Macmillan Publishers Limited. All rights reserved

7. Williams, T. F., Mirando, A. C., Wilkinson, B., Francklyn, C. S. & Lounsbury, K. M. Secreted Threonyl-tRNA synthetase stimulates endothelial cell migration and angiogenesis. *Sci. Rep.* **3,** 1317 (2013).
8. Park, M. C. *et al.* Secreted human glycyl-tRNA synthetase implicated in defense against ERK-activated tumorigenesis. *Proc. Natl Acad. Sci. USA* **109,** E640–E647 (2012).
9. Guo, M., Yang, X. L. & Schimmel, P. New functions of aminoacyl-tRNA synthetases beyond translation. *Nature Rev. Mol. Cell Biol.* **11,** 668–674 (2010).
10. Lee, H. J. *et al.* Two novel mutations of GARS in Korean families with distal hereditary motor neuropathy type V. *J. Peripher. Nerv. Syst.* **17,** 418–421 (2012).
11. Motley, W. W., Talbot, K. & Fischbeck, K. H. GARS axonopathy: not every neuron's cup of tRNA. *Trends Neurosci.* **33,** 59–66 (2010).
12. Kawakami, N. *et al.* A novel mutation in glycyl-tRNA synthetase caused Charcot-Marie-Tooth disease type 2D with facial and respiratory muscle involvement. *Rinsho Shinkeigaku* **54,** 911–915 (2014).
13. Sun, A. *et al.* A novel mutation of the glycyl-tRNA synthetase (GARS) gene associated with Charcot–Marie–Tooth type 2D in a Chinese family. *Neurol. Res.* **37,** 782–787 (2015).
14. Achilli, F. *et al.* An ENU-induced mutation in mouse glycyl-tRNA synthetase (GARS) causes peripheral sensory and motor phenotypes creating a model of Charcot-Marie-Tooth type 2D peripheral neuropathy. *Dis. Model. Mech.* **2,** 359–373 (2009).
15. Seburn, K. L., Nangle, L. A., Cox, G. A., Schimmel, P. & Burgess, R. W. An active dominant mutation of glycyl-tRNA synthetase causes neuropathy in a Charcot-Marie-Tooth 2D mouse model. *Neuron* **51,** 715–726 (2006).
16. Motley, W. W. *et al.* Charcot-Marie-Tooth-linked mutant GARS is toxic to peripheral neurons independent of wild-type GARS levels. *PLoS Genet.* **7,** e1002399 (2011).
17. He, W. *et al.* Dispersed disease-causing neomorphic mutations on a single protein promote the same localized conformational opening. *Proc. Natl Acad. Sci. USA* **108,** 12307–12312 (2011).
18. Del Bo, R. *et al.* Coexistence of CMT-2D and distal SMA-V phenotypes in an Italian family with a *GARS* gene mutation. *Neurology* **66,** 752–754 (2006).
19. Dubourg, O. *et al.* The G526R glycyl-tRNA synthetase gene mutation in distal hereditary motor neuropathy type V. *Neurology* **66,** 1721–1726 (2006).
20. Schwarz, Q. *et al.* Vascular endothelial growth factor controls neuronal migration and cooperates with Sema3A to pattern distinct compartments of the facial nerve. *Genes Dev.* **18,** 2822–2834 (2004).
21. Huber, A. B. *et al.* Distinct roles for secreted semaphorin signaling in spinal motor axon guidance. *Neuron* **48,** 949–964 (2005).
22. Song, M. R. *et al.* T-Box transcription factor Tbx20 regulates a genetic program for cranial motor neuron cell body migration. *Development* **133,** 4945–4955 (2006).
23. Lewcock, J. W., Genoud, N., Lettieri, K. & Pfaff, S. L. The ubiquitin ligase Phr1 regulates axon outgrowth through modulation of microtubule dynamics. *Neuron* **56,** 604–620 (2007).
24. Mackenzie, F. & Ruhrberg, C. Diverse roles for VEGF-A in the nervous system. *Development* **139,** 1371–1380 (2012).
25. Oosthuyse, B. *et al.* Deletion of the hypoxia-response element in the vascular endothelial growth factor promoter causes motor neuron degeneration. *Nature Genet.* **28,** 131–138 (2001).
26. Wang, L. J. *et al.* Neuroprotective effects of glial cell line-derived neurotrophic factor mediated by an adeno-associated virus vector in a transgenic animal model of amyotrophic lateral sclerosis. *J. Neurosci.* **22,** 6920–6928 (2002).
27. Acsadi, G. *et al.* Increased survival and function of SOD1 mice after glial cell-derived neurotrophic factor gene therapy. *Hum. Gene Ther.* **13,** 1047–1059 (2002).
28. Kaspar, B. K., Lladó, J., Sherkat, N., Rothstein, J. D. & Gage, F. H. Retrograde viral delivery of IGF-1 prolongs survival in a mouse ALS model. *Science* **301,** 839–842 (2003).
29. Nayak, M. S., Kim, Y. S., Goldman, M., Keirstead, H. S. & Kerr, D. A. Cellular therapies in motor neuron diseases. *Biochim. Biophys. Acta* **1762,** 1128–1138 (2006).
30. Azzouz, M. *et al.* VEGF delivery with retrogradely transported lentivector prolongs survival in a mouse ALS model. *Nature* **429,** 413–417 (2004).

Supplementary Information is available in the online version of the paper.

Acknowledgements We thank P. Schimmel, J. Dolkas, C. Farrokhi, L. Lisowski, C. Ly, S. Chalasani, T. Liu, Q. Hu, P. Li, N. Sheng and members of The Scripps Laboratories of tRNA Synthetase Research and the Pfaff laboratory for advice and discussions on the experiments and manuscript. We are grateful to S. Ackerman, K.-F. Lee, D. O'leary and D. Ginty for providing mouse lines. W.H., H.Z. and N.W. were supported by fellowships from the National Foundation for Cancer Research. G.B. was supported by the Pioneer fund and Howard Hughes Medical Institute. S.L.P. is a Howard Hughes Medical Institute investigator and a Benjamin H. Lewis chair in Neuroscience. This research is supported by grants from the US National Institutes of Health (R01GM088278, R21NS084254 and R01NS054154), The Marshall Heritage Foundation and the Sol Goldman Trust, and by aTyr Pharma through an agreement with The Scripps Research Institute.

Author Contributions W.H., G.B., S.L.P. and X.-L.Y. designed the study, analysed the data, and prepared the manuscript. W.H. carried out molecular cloning, binding analyses, secretion studies, and other biochemical experiments. G.B. performed the mouse genetics, viral injections, behaviour testing, and histology experiments. H.Z. carried out Nrp1 domain mapping, GlyRS–VEGF competition, and additional pull-down assays, and contributed to study design and figure preparation. N.W. performed co-immunoprecipitation to detect aberrant GlyRS–Nrp1 interaction using CMT2D patient samples. A.J. and V.G. provided transformed lymphocytes samples from CMT2D patients. J.L. and P.R.G. performed the hydrogen–deuterium exchange analysis. N.M.W. and K.L. assisted with mouse studies. Y.S. and C.D.D. contributed to biochemical experiments. H.L. and V.S. contributed to histology experiments. R.W.B. provided mice, technical support, and scientific advice.

Author Information Reprints and permissions information is available at www.nature.com/reprints. The authors declare competing financial interests: details are available in the online version of the paper. Readers are welcome to comment on the online version of the paper. Correspondence and requests for materials should be addressed to X.-L.Y. (xlyang@scripps.edu) or S.L.P. (pfaff@salk.edu)

©2015 **Macmillan Publishers Limited. All rights reserved**

METHODS

Mice. The following strains of mice were used in this study: wild-type C57BL/6J (JAX), P234KY-CMT2D mutant (background includes a mix of C57BL/6, CB6 and CAST)[14], Tg (Hb9:GFP)[31], Tg (Isl^{MN}:GFP-F)[23], Nrp1 mutant[32], TrkB mutant[33], Robo1 mutant[34], Dcc mutant[35], and Unc5C mutant[36]. Both male and female mice were used in this study. All experiments were done in accordance with Institutional Animal Care and Use Committee animal protocols and BSL2+ safety protocols, on animals housed in groups on a 12-h light–dark cycle.

Recombinant GlyRS expression and purification. Carboxy-terminal His-tagged human $GlyRS^{WT}$ and $GlyRS^{CMT2D}$ proteins were individually cloned into pET21b vector (Novagen) and expressed in *Escherichia coli* BL21 (DE3) host cells at 25 °C. The proteins were purified by Ni-NTA agarose affinity column followed by ion-exchange monoQ column and size-exclusion column Superdex 200 (GE Healthcare). To prepare non-tagged human $GlyRS^{WT}$ and $GlyRS^{CMT2D}$ proteins, the *GARS* gene was fused with an amino-terminal His-SUMO tag, cloned into pET28a vector (Novagen), and expressed as His-SUMO-GlyRS fusion proteins in *Escherichia coli* BL21 (DE3) cells. The fusion proteins were purified with a Ni-NTA agarose affinity column, and then subjected to homemade Ulp1 protease to remove the His-SUMO tag. The non-tagged GlyRS proteins were separated from the tag by flowing through the Ni-NTA column again.

Hydrogen–deuterium exchange analysis. Solution-phase amide hydrogen–deuterium exchange (HDX) was performed with a fully automated system as described previously[37]. Briefly, 4 µl of His-tagged $GlyRS^{P234KY}$ or $GlyRS^{WT}$ was diluted to 20 µl with D_2O-containing HDX buffer to a final concentration of 10 µM, and incubated at 4 °C for 10, 30, 60, 900, and 3,600 s. Following on-exchange, unwanted back exchange was minimized by adding 30 µl of 1% TFA in 5 M urea to denature the protein (held at 1 °C). Samples were then passed across an immobilized pepsin column (prepared in house) at 50 µl min^{-1} (0.1% TFA, 15 °C), and the resulting peptides were trapped onto a C8 trap cartridge (Thermo Fisher, Hypersil Gold). Peptides were eluted across a 1 mm × 50 mm C18 high-performance liquid chromatography (HPLC) column (Hypersil Gold, Thermo Fisher) with a 4–40% CH_3CN gradient and 0.3% formic acid over 5 min at 2 °C, and electrosprayed directly into an Orbitrap mass spectrometer (LTQ Orbitrap with ETD; Thermo Fisher). Data were processed with in-house software[38] and visualized with PyMOL (DeLano Scientific). The difference in HDX between $GlyRS^{P234KY}$ and $GlyRS^{WT}$ was calculated by subtracting the average percentage deuterium uptake for $GlyRS^{P234KY}$ from that for $GlyRS^{WT}$ after 10, 30, 60, 300, 900 and 3,600 s of on-exchange. Please note that we cannot directly compare the numbers obtained here for $GlyRS^{P234KY}$ with those for other $GlyRS^{CMT2D}$ mutants from the previous study[17], because this and the precious analysis were carried out in two different laboratories with different instruments and experimental procedures.

Detection of GlyRS proteins in cell cultures. NSC-34 motor neuron cells (Cellutions Biosystems) and C2C12 mouse adherent myoblasts (from A. Patapoutian's laboratory at The Scripps Research Institute) were maintained in DMEM supplemented with 10% heat-inactivated fetal bovine serum (FBS) and 1% penicillin (Life Technologies) at 37 °C in a humidified incubator containing 5% CO_2. These cell lines had not been recently authenticated and tested for mycoplasma contamination. Myogenic differentiation of C2C12 myoblasts was induced by substituting the FBS with 2% horse serum. The cells were further cultured in Opti-MEM Reduced Serum Medium (Life Technologies) for 16 h. Brefeldin A (Cell Signaling Technology), GW4869 (Sigma-Aldrich), or monensin (eBioscience) was added to the cell medium for 2 h before the cells and the medium were separated for western blot analysis. After removal of cell debris by spinning the medium at 300*g* for 10 min, the supernatant was concentrated using Amicon Ultra-4 Centrifugal filter (Millipore). Cells were lysed using cell lysis buffer (ATCC) with added protease inhibitor cocktail (Roche). The following antibodies were used for western blot analysis: mouse anti-GlyRS (H00002617-B01P, Abnova; 1:1,000), rabbit anti-GAPDH (#3683, Cell Signaling Technology; 1:1,000), rabbit anti-vWF (sc-14014, Santa Cruz; 1:50), and rabbit anti-TSG101 (MABC649, Millipore; 1:1,000). To study the effect of CMT2D-causing mutation on GlyRS secretion, constructs overexpressing V5-tagged $GlyRS^{P234KY}$ or $GlyRS^{WT}$ were transfected into COS7 cells using lipofectamine 2000 (Invitrogen). The expression and secretion of GlyRS proteins were detected by western blot analysis using anti-V5 antibody (R960-25, Invitrogen; 1:5,000).

Exosome purification and analysis. The general idea of exosome purification by differential centrifugation is depicted in Extended Data Fig. 3a. Supernatants from NSC-34 cell media were subjected to successive centrifugation steps at 4 °C: (1) 200*g* for 10 min to eliminate floating cells; (2) 2,000*g* for 10 min to discard large dead cells; (3) 10,000*g* for 1 h to remove cell debris and cellular organelles such as mitochondria and lysosomes. At each step, the pellet was thrown away and the supernatant was used for the following step. The final supernatant was centrifuged at 100,000*g* at 4 °C for 4 h to pellet micro-vesicles that are commonly known as 'exosomes'. The final supernatant and the exosome fraction were analysed by western blot analysis using the antibodies specified earlier and rabbit anti-Bip antibody (#3183S, Cell Signaling; 1:1,000).

***In vitro* pull-down assay.** Recombinant rat Nrp1–Fc, mouse TrkB–Fc, mouse Dcc–Fc, rat Robo1–Fc and human Unc5c–Fc extracellular domain–Fc chimaeras (R&D systems) were bound to Protein G beads. Purified non-tagged $GlyRS^{WT}$ and $GlyRS^{CMT2D}$ proteins were individually added to the receptor-immobilized beads and incubated for 1 h at 4 °C. After removal of unbound GlyRS proteins, SDS-loading buffer was directly added to the beads to elute the receptor and its bound GlyRS. The amount of GlyRS bound to receptors was analysed by western blot analysis using mouse anti-GlyRS antibodies (H00002617-B01P, Abnova; 1:1,000).

Co-immunoprecipitation and western blot analysis using mouse tissues. The interaction between endogenous GlyRS and Nrp1 proteins was detected by co-immunoprecipitation. Adult mouse neural samples were lysed using RIPA buffer (Cell Signaling) containing 20 mM Tris-HCl (pH 7.5), 150 mM NaCl, 1 mM Na_2EDTA, 1 mM EGTA, 1% NP-40, 1% sodium deoxycholate, 2.5 mM sodium pyrophosphate, 1 mM β-glycerophosphate, 1 mM Na_3VO_4, and 1 µg ml^{-1} leupeptin. Immunoprecipitation was performed with rabbit anti-Nrp1 antibody (NBP1 40666, Novus Biologicals; 1:100) and the precipitates were subjected to western blot analysis using mouse anti-GlyRS antibody (H00002617-B01P, Abnova; 1:1,000).

Western blot was performed to analyse the expression levels of various neuronal proteins in E12.5 wild-type and CMT2D mutant neural tissues. The following primary antibodies were used: mouse anti-GlyRS (H00002617-B01P, Abnova; 1:1,000), rabbit anti-Nrp1 (#3725S, Cell Signaling; 1:1,000), rabbit anti-VEGFR1 (#36-1100, Life Technologies; 1:1,000), rabbit anti-VEGFR2 (#2479S, Cell Signaling; 1:1,000), mouse anti-β-actin (#3700, Cell Signaling; 1:1,000), mouse anti-Dcc (AF5, Abcam; 1:100), rabbit anti-Robo1 (NB100-60458, Novus Biologicals; 1:2,000), mouse anti-NF (2H3, DSHB; 1:100), mouse anti-MAP2 (MAB364, Millipore; 1:500), rabbit anti-GAP43 (AB5220, Millipore; 1:1,000), and rabbit anti-β-catenin (#9587, Cell Signaling; 1:1,000).

Co-immunoprecipitation using CMT2D patient samples. Peripheral blood was drawn from CMT2D patients carrying the L129P mutation and control individuals after obtaining their written informed consent. The study complies with the ethical guidelines of the Medical University of Sofia, Bulgaria and University of Antwerp, Belgium. Lymphocytes were isolated on a Ficoll–Paque gradient, transformed with Epstein–Barr virus and incubated at 37 °C for 2 h. After centrifugation, cells were re-suspended in 4 ml RPMI complete medium (Life Technologies) supplemented with 1% phytohaemagglutinin. Cells were seeded on a 24-well plate and incubated at 37 °C, 6% CO_2 for a minimum of 3 days. After establishment, cell lines were cultivated in RPMI1640 medium containing 15% fetal calf serum, 1% sodium pyruvate, 1% 200 M L-glutamine and 2% penicillin/streptomycin. The harvested lymphoblastoid cells were lysed using RIPA buffer (Cell Signaling). Immunoprecipitation was performed with rabbit anti-Nrp1 antibody (Novus Biologicals) and rabbit anti-IgG (#2729, Cell Signaling) and the pull-down samples were subjected to western blot analysis using rabbit anti-GlyRS antibody (sc-98614, Santa Cruz Biotechnology; 1:500).

Mapping of $GlyRS^{CMT2D}$ interaction domain on Nrp1. The variants of Nrp1 extracellular domain (ECD) include intact ECD (residues Arg 23–Asp 840), b1b2c domain (residues Phe 273–Asp 840), a1a2 domain (residues Arg 23–Asp 272), b1b2 domain (residues Phe 273–Phe 643), c domain (residues Thr 589–Asp 840), b1 domain (residues Phe 273–Asp 428) and b2 domain (residues Lys 425–Phe 643). These variants were designed as chimaera proteins containing a 17-residue secretion signal peptide from myeloid cell surface antigen CD33 (gp67) at the N terminus and a human IgG Fc domain at C terminus, and were expressed using pcDNA6.0/V5-His-A vector (Life Technologies). For each Nrp1 variants, 3 µg plasmids were transfected using Lipofactmine 2000 (Life Technologies) into human HEK293 cells in a 6-well plate. Twenty hours after transfection, MEM media containing secreted Nrp1 variants were collected and incubated with 30 µl Protein A resins. The Nrp1-bound resins were divided equally into two 1.5 ml Eppendorf tubes and incubated with 5 µg of recombinant $GlyRS^{CMT2D}$ or $GlyRS^{WT}$ in 1 ml of Washing Buffer (PBS, 5 mM β-ME, 0.2% BSA and 0.05% Triton X-100) for 1 h. Resins were then washed three times with the Washing Buffer and once with PBS. The bound proteins were eluted with 30 µl of SDS–PAGE sample buffer and subjected to western blotting analysis using mouse anti-GlyRS (H00002617-B01P, Abnova; 1:1,000) and rabbit anti-His antibodies (RHIS-45P-Z, ICL Lab; 1:10,000) to detect GlyRS and the Nrp1 variants, respectively.

The b1 (residues Phe 273–Asp 428), b2 (residues Lys 425–Glu 586), and b1b2 domain (residues Phe 273–Glu 586) of Nrp1 fused with an N-terminal glutathione *S*-transferase (GST) tag was cloned into the pET28a vector (Novagen), expressed in *E. coli* BL21(DE3) cells and purified with GST resin (Qiagen). GST or GST–Nrp1 fusion proteins was incubated with 20 µl GST resin and then bind with non-tagged wild-type or P234KY GlyRS in 1 ml of Washing Buffer (1×PBS,

©2015 Macmillan Publishers Limited. All rights reserved

5 mM BME, 0.2% BSA and 0.05% Triton X-100) for 1 h. GST resins were washed three times with Washing Buffer and once more with PBS. The bound proteins were eluted with SDS–PAGE sample buffer, and subjected to western blotting analysis.

Competition assay between VEGF-A_{165} and $GlyRS^{CMT2D}$ for Nrp1 binding. In each experiment, 5 μg of GST–b1b2 protein was bound with 15 μl of GST resin in 1 ml Washing Buffer on ice. The competition was tested in both directions. In one direction, 30 nM of P234KY $GlyRS^{CMT2D}$ was added to GST–b1b2 with an increasing concentration of human VEGF-A_{165} (IBL); in the opposite direction, 30 nM of VEGF-A_{165} was added with an increasing concentration of P234KY $GlyRS^{CMT2D}$. After the resins were washed three times with the Washing Buffer and once with PBS, proteins were eluted with SDS–PAGE sample buffer, and analysed by western blot using rabbit anti-VEGF-A (ABS82, Millipore; 1:2,000), mouse anti-GlyRS (H00002617-B01P, Abnova; 1:1,000) and rabbit anti-GST (#2622, Cell Signaling; 1:1,000) antibodies.

Immunostaining and imaging. Immunostaining of NMJs was performed as described[14]. Cocktails of the following primary antibodies were used to visualize nerves: rabbit anti-NF (AB1991, Millipore; 1:1,000), rabbit anti-synaptophysin (A0010, Dako; 1:2,000), and mouse anti-SV2 (DSHB; 1:1,000). Secondary antibodies were Alexa-488 or -647 conjugated (Molecular Probes/Invitrogen; 1:1,000). Tetramethylrhodamine-conjugated α-bungarotoxin (T-1175, Molecular Probes/Invitrogen; 1:1,000) was used to visualize acetylcholine receptors (AChRs) on muscles. The occupancy of NMJs is measured by examining the overlap of the motor nerve terminal (green) with AChRs on the muscle (red). At least 40 randomly selected NMJs were examined from each of three mutant and three control mice. The flat-mount preparations of hindbrains were performed as previously described[23]. Rabbit anti-Isl1/2 (ref. 39) was used to label facial motor nuclei by whole-mount immunostaining. The distance between the facial motor nucleus and trigeminal nucleus was measured for each embryo. Each distance was further normalized to the relative distance of the wild-type facial motor nucleus. Rabbit anti-VEGF (ab52917, Abcam; 1:200) was used to determine the expression of VEGF in muscle fibres.

Bright-field and fluorescence images of whole embryos were obtained using a 0.8× objective on Zeiss Lumar.V12 fluorescence stereomicroscope. Confocal images were obtained using 10× and 20× objectives on Olympus Fluoview 1000 confocal microscope.

Hindlimb extension test. Mice were suspended by the tail and the extent of hindlimb extension was observed over 10 s. A score of 2 corresponded to a normal extension reflex in hindlimbs with splaying of toes. A score of 1 corresponded to clenching of hindlimbs to the body with partial splaying of toes. A score of 0 corresponded to clasping hindlimbs with curled toes. Three tests were performed for each mouse with 5 s intervals. A score of 1.5 or 0.5 corresponded to behaviours between 2 and 1, or between 1 and 0, respectively.

Footprint test. Blue ink was applied to the hind paws of each mouse and the animal was placed in a narrow alley (9 × 80 × 25 cm) with the floor covered with white paper. A home cage was placed at the end of the alley for the animal to walk to while leaving its footprints on the paper. Stride length was assessed by measuring the average distances of at least three consecutive steps on each side.

Inclined plane test. Hindlimb strength was assessed at postnatal 4 weeks using the inclined plane test. Briefly, animals were placed on an inclined plane, and the angle of incline was gradually increased starting from 15°. The maximum angle at which the animal could maintain its position for 5 s constituted the inclined plane score. The test was performed three times for each mouse.

Rotarod test. Motor coordination was assessed with a rotarod apparatus (Economex, Columbus Instruments). The mice were first placed on the stationary rod (0 r.p.m.) to acclimate them to the apparatus, followed by a trial at a rotation speed of 1 r.p.m. for 3 min or until a fall occurred. For testing, the rotation of the rotarod was accelerated from 0 r.p.m. with an accelerating rate (0.1 r.p.m. min^{-1}). The latency of each mouse to fall was monitored for three consecutive trials and the intra-trial interval for each animal was about 20 min. The average time of three trials was used as a measure of motor performance.

Virus preparation and injection. The complementary DNAs encoding GDNF, VEGF-A_{121} or VEGF-A_{165} were cloned into lentiviral vector (p156RRLsin PPTCMVGFPPRE) between BamHI and SalI sites. All lentiviruses were produced by the GT3 core facility at the Salk Institute with a titre of 1×10^{12}–2×10^{13} genome copies per ml. Injections were performed at P5 (± 1 day) after anaesthetizing pups on ice. Multiple injections ($n \geq 8$) of virus (5 μl for each limb) into a variety of hindlimb muscles were performed with a Hamilton syringe. On the basis of the expression pattern of GFP reporter, we found that the lentiviruses mainly infect muscle fibres.

Nerve histology and imaging. Mouse sciatic nerves were dissected and fixed in 2.5% glutaraldehyde in 0.1 M phosphate buffer. Nerve samples were then osmicated, dehydrated and embedded in araldite resin. Transverse nerve sections (1 μm) were cut on a Leica RM2065 microtome and stained with methylene blue Azure II. Images were collected on a Leica DMR microscope or an Olympus BX61 microscope. Axon numbers were determined from two non-overlapping fields (50 × 50 μm) from each of three mutant and three control nerve samples. Axon diameters were measured by Image J.

Statistics. All graphs and data generated in this study were analysed using GraphPad Prism 6.0 Software (MacKiev) or Excel (Microsoft). Two-tailed unpaired *t*-tests with Welch's correction using parametric distribution, two-tailed Mann–Whitney test using unparametric distribution, or two-tailed paired Wilcoxon test using unparametric distribution were performed to measure differences from at least three independent biological replicates. $P < 0.05$ was considered significant. These tests do not require similar variance of the data between the groups that are being statistically compared. The normality of the data was determined by D'Agostino-Pearson omnibus test and Kolmogorov–Smirnov test. No statistical methods were used to predetermine sample sizes, but our sample sizes are similar to those generally used in the field.

For all animal studies, analyses were performed on approximately equal numbers of male and female mice selected randomly from populations, and no sex-specific differences in the disease progression were identified. All behavioural experiments were performed in double-blind fashion, and stressed animals were excluded from the analysis.

31. Lee, S. K., Jurata, L. W., Funahashi, J., Ruiz, E. C. & Pfaff, S. L. Analysis of embryonic motoneuron gene regulation: derepression of general activators function in concert with enhancer factors. *Development* **131,** 3295–3306 (2004).
32. Gu, C. *et al.* Neuropilin-1 conveys semaphorin and VEGF signaling during neural and cardiovascular development. *Dev. Cell* **5,** 45–57 (2003).
33. Xu, B. *et al.* Cortical degeneration in the absence of neurotrophin signaling: dendritic retraction and neuronal loss after removal of the receptor TrkB. *Neuron* **26,** 233–245 (2000).
34. Ma, L. & Tessier-Lavigne, M. Dual branch-promoting and branch-repelling actions of Slit/Robo signaling on peripheral and central branches of developing sensory axons. *J. Neurosci.* **27,** 6843–6851 (2007).
35. Fazeli, A. *et al.* Phenotype of mice lacking functional *Deleted in colorectal cancer* (*Dcc*) gene. *Nature* **386,** 796–804 (1997).
36. Burgess, R. W., Jucius, T. J. & Ackerman, S. L. Motor axon guidance of the mammalian trochlear and phrenic nerves: dependence on the netrin receptor Unc5c and modifier loci. *J. Neurosci.* **26,** 5756–5766 (2006).
37. Chalmers, M. J. *et al.* Probing protein ligand interactions by automated hydrogen/deuterium exchange mass spectrometry. *Anal. Chem.* **78,** 1005–1014 (2006).
38. Pascal, B. D. *et al.* HDX workbench: software for the analysis of H/D exchange MS data. *J. Am. Soc. Mass Spectrom.* **23,** 1512–1521 (2012).
39. Ericson, J., Thor, S., Edlund, T., Jessell, T. M. & Yamada, T. Early stages of motor neuron differentiation revealed by expression of homeobox gene Islet-1. *Science* **256,** 1555–1560 (1992).
40. Savina, A., Furlán, M., Vidal, M. & Colombo, M. I. Exosome release is regulated by a calcium-dependent mechanism in K562 cells. *J. Biol. Chem.* **278,** 20083–20090 (2003).
41. Soo, C. Y. *et al.* Nanoparticle tracking analysis monitors microvesicle and exosome secretion from immune cells. *Immunology* **136,** 192–197 (2012).

©2015 Macmillan Publishers Limited. All rights reserved

Extended Data Figure 1 | Hydrogen–deuterium exchange analysis to compare GlyRS^{CMT2D}(P234KY) and GlyRS^{WT} in solution. A global increase (15%) in deuterium incorporation for the mutant GlyRS was observed, indicating overall structural opening. The regions having significant changes (>10%) in deuterium incorporation are highlighted under the human cytosolic GlyRS sequence with different colour codes (see box).

©2015 Macmillan Publishers Limited. All rights reserved

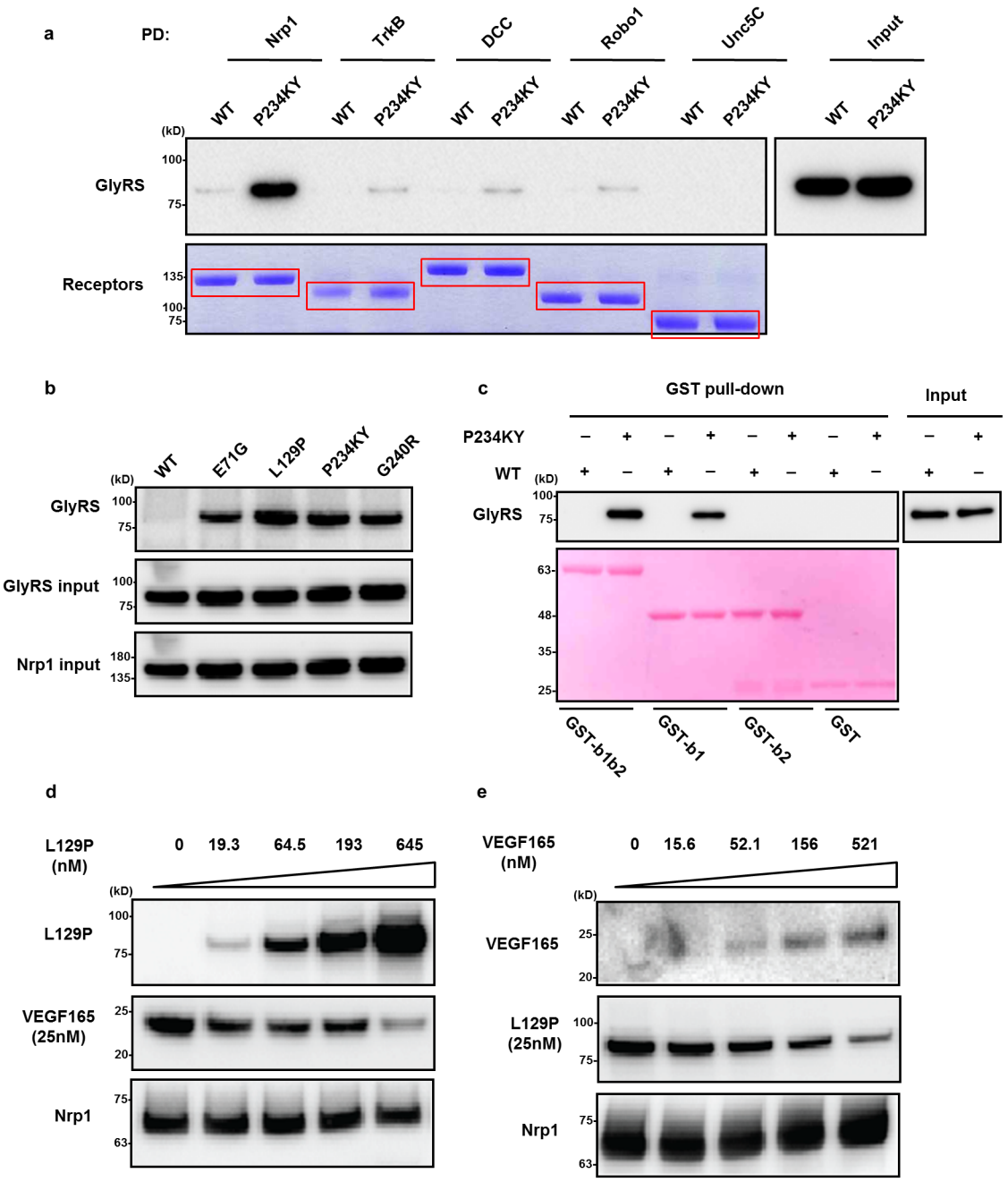

Extended Data Figure 2 | Characterization of the binding activity of GlyRS^{CMT2D}. **a**, *In vitro* pull-down of GlyRS^{CMT2D}(P234KY) proteins with the ectodomains of Nrp1, TrkB, Dcc, Robo1 and Unc5C proteins. Note the much stronger binding of GlyRS^{CMT2D} with Nrp1 compared with other receptors. GlyRS was detected by immunoblot with anti-GlyRS antibody; similar amounts of input receptors were visualized by Coomassie blue staining. **b**, *In vitro* pull-down of GlyRS^{CMT2D} proteins with the ectodomain of Nrp1. In addition to L129P and P234KY, direct binding to Nrp1 was detected for E71G and G240R GlyRS^{CMT2D}. **c**, GST pull-down to confirm that b1 domain of Nrp1 is the main binding site of GlyRS^{CMT2D}. The amount of GST and GST fusion proteins used for GlyRS^{CMT2D} binding was visualized by Ponceau staining. **d**, **e**, *In vitro* pull-down assay showing the mutual competition between GlyRS^{CMT2D}(L129P) and VEGF-A$_{165}$ for Nrp1 binding.

©2015 Macmillan Publishers Limited. All rights reserved

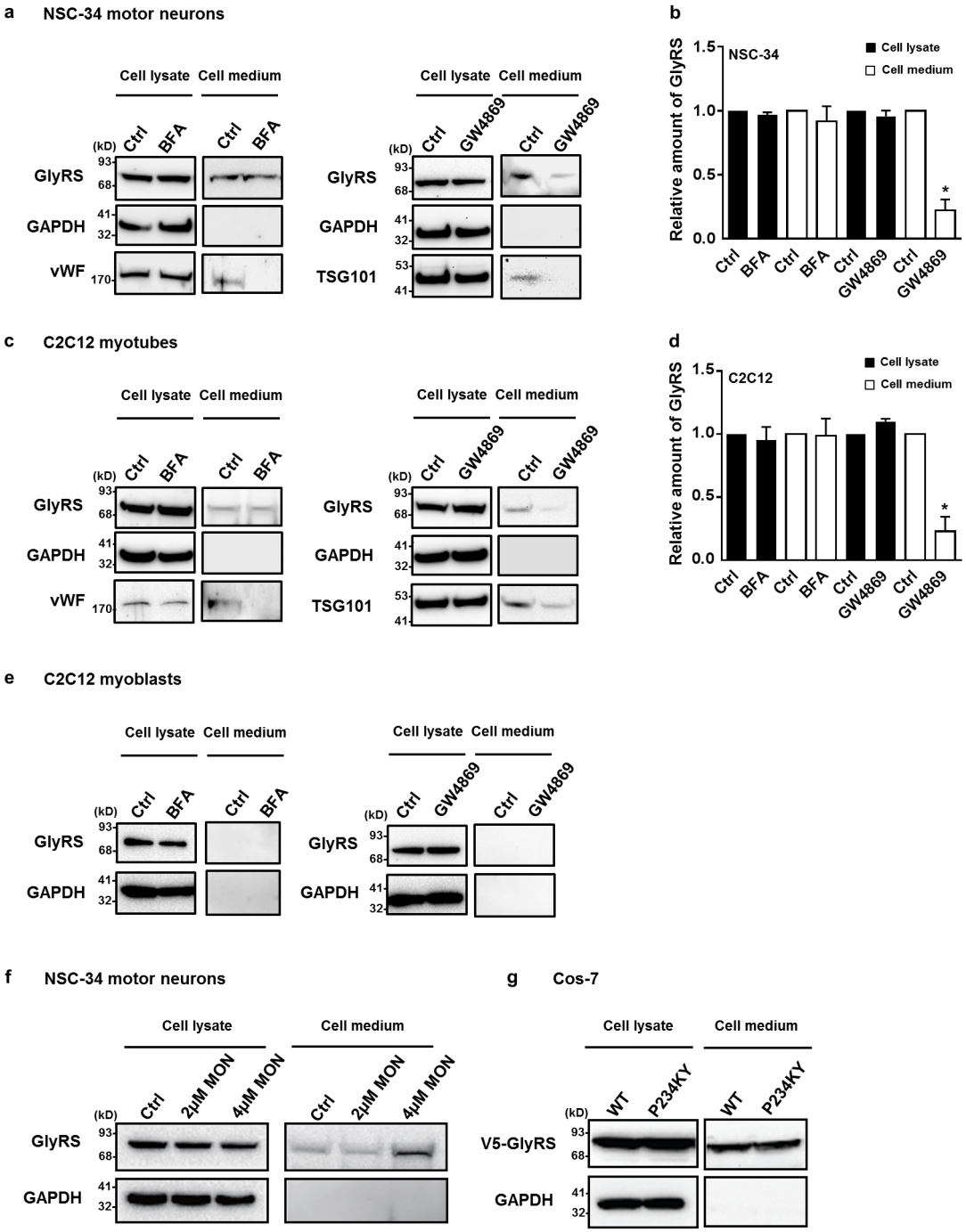

Extended Data Figure 3 | Detection of GlyRS proteins in the cell medium. **a**, **c**, **e**, Western blot analysis of the GlyRS protein levels in NSC-34 motor neurons (**a**), C2C12 cell-differentiated myotubes (**c**) and undifferentiated C2C12 myoblasts (**e**). The observation that differentiated myotubes also secrete GlyRS raises the possibility that muscles, which are directly innervated by the peripheral motor neurons, might contribute to the disease pathology. The level of GlyRS proteins in cell medium is diminished by application of the exosome-pathway inhibitor GW4869, but not by brefeldin A (BFA), an inhibitor of the classical endoplasmic reticulum (ER)-to-Golgi secretory pathway. GAPDH (cytoplasmic protein), vWF (secretory protein through ER–Golgi pathway) and TSG101 (exosomal protein) are used as controls. **b**, **d**, Quantification of GlyRS protein level indicated in **a**, **c**. Data are presented as the mean ± s.e.m. of three independent experiments ($*P < 0.05$, *t*-test). **f**, Western blot analysis of the GlyRS protein level in NSC-34 motor neurons. The level of GlyRS proteins in the cell medium is increased by the treatment of monensin (MON), an activator for microvesicle release by regulating the intracellular calcium level[40,41]. Vehicle-treated cells were used as control (Ctrl). **g**, Western blot analysis of the GlyRS protein level in Cos7 cells transfected with plasmids encoding $GlyRS^{WT}$ and $GlyRS^{CMT2D}$(P234KY). The expression of GlyRS proteins was detected by immunoblot with antibody to V5 epitope tag. GAPDH was used as control. Note the similar level of $GlyRS^{CMT2D}$ and $GlyRS^{WT}$ in the media of transfected Cos7 cells.

©2015 Macmillan Publishers Limited. All rights reserved

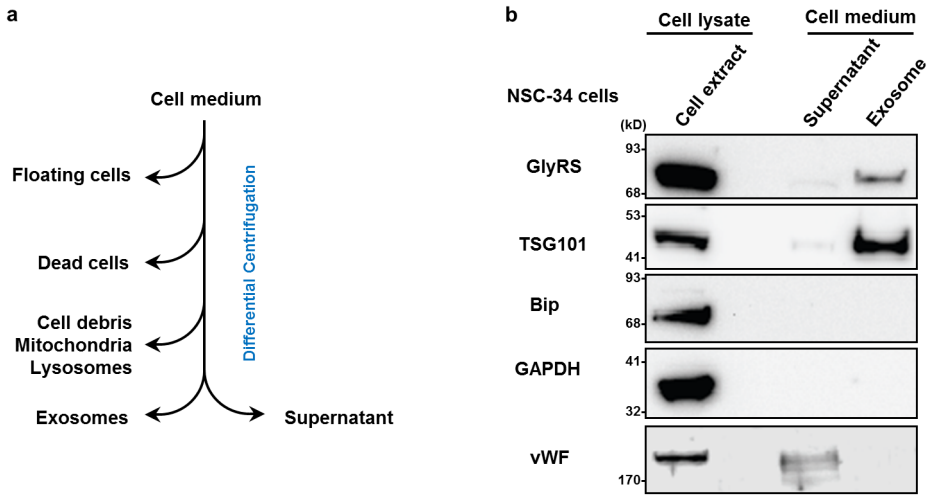

Extended Data Figure 4 | Detection of GlyRS proteins in exosome-enriched fractions. **a**, Diagram showing the procedure of exosome separation from the cell medium of NSC-34 cells by differential centrifugation. See Methods for details. **b**, Western blot analysis of proteins associated with various fractions. GlyRS proteins were detected in the exosome-enriched fractions but not in supernatant fractions. The quality of the exosome preparation was controlled by detection of TSG101 (exosomal protein), Bip (ER-associated protein), GAPDH (cytoplasmic protein), and vWF (secretory protein through ER–Golgi pathway).

©2015 Macmillan Publishers Limited. All rights reserved

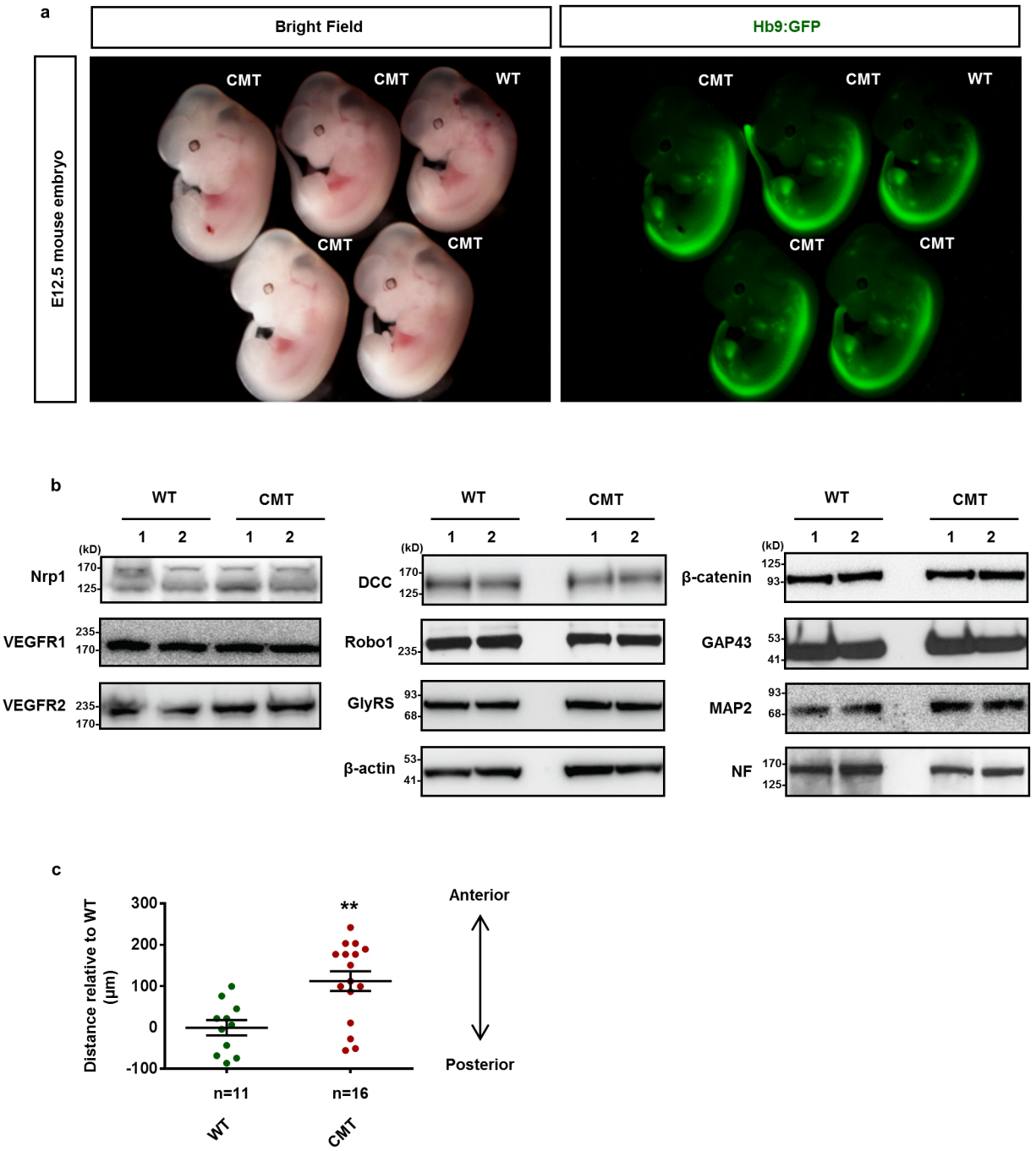

Extended Data Figure 5 | CMT2D mutant embryos have overall normal morphology but exhibit facial motor neuron migration defects. **a**, Lateral view of wild-type and CMT2D mutant embryos at E12.5. Motor neurons are specifically labelled by a transgenic fluorescence reporter, Hb9:GFP (green). Note overall normal morphology of CMT2D mutant embryos (CMT) compared with their littermate controls (wild type). **b**, Western bolt analysis of protein expression in E12.5 mouse neural tissues. The expression levels of various neuronal proteins appear normal in CMT2D mutants compared with their littermate controls. **c**, Considering CMT2D mutants show varying degrees of morphological change of facial motor nucleus, the facial motor neuron migration phenotype is quantified by measuring the relative distance of the facial motor nucleus between wild-type and CMT littermate embryos (each dot represents one facial motor nucleus, $n = 6$ embryos for wild type; $n = 8$ embryos for CMT2D). We find that the migration of facial motor neurons is significantly disrupted in CMT embryos. Data are presented as the mean ± s.e.m. $^{**}P < 0.01$ (*t*-test).

©2015 Macmillan Publishers Limited. All rights reserved

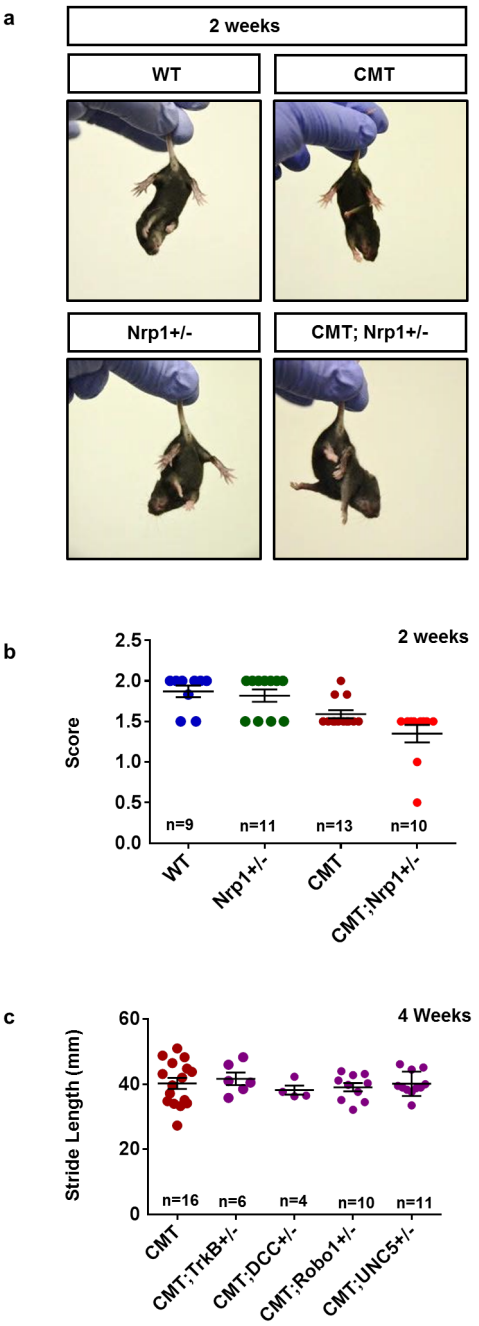

Extended Data Figure 6 | Genetic interaction between *Gars* and *Nrp1* in the early stage of CMT2D. **a**, **b**, Hindlimb extension test of wild-type and mutant animals at 2 weeks. Note that two out of nine $Gars^{CMT2D}$;$Nrp1^{+/-}$ (CMT;$Nrp1^{+/-}$) mutants exhibit hindlimb weakness with significantly lower scores compared with $Gars^{CMT2D}$ (CMT), $Nrp1^{+/-}$ and wild-type littermate controls. **c**, Comparison of stride lengths in different CMT2D mutant mice at 4 weeks old: $Gars^{CMT2D}$ (CMT), $Gars^{CMT2D}$;$TrkB^{+/-}$ (CMT;$TrkB^{+/-}$), $Gars^{CMT2D}$;$Dcc^{+/-}$ (CMT;$Dcc^{+/-}$), $Gars^{CMT2D}$;$Robo1^{+/-}$ (CMT;$Robo1^{+/-}$), and $Gars^{CMT2D}$;$Unc5C^{+/-}$ (CMT;$Unc5C^{+/-}$). No significant differences were observed between compound heterozygotes and their littermate controls (CMT).

©2015 Macmillan Publishers Limited. All rights reserved

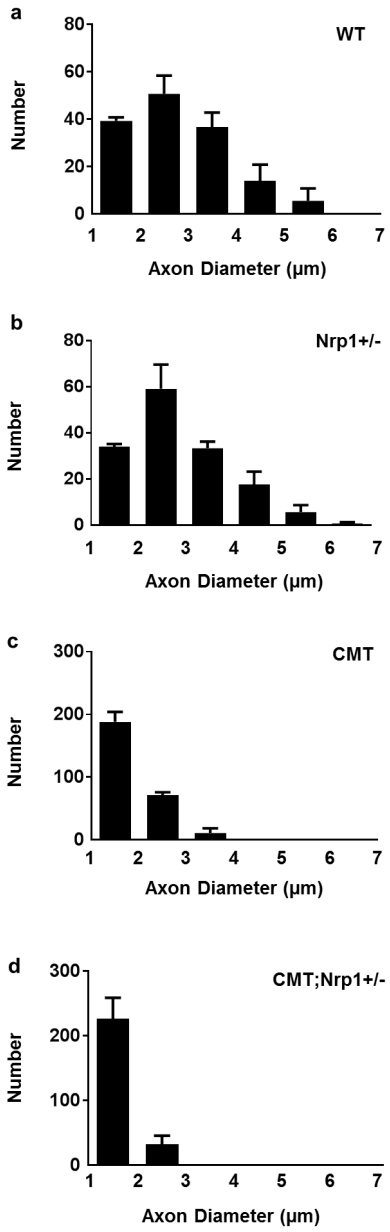

Extended Data Figure 7 | Axonal dystrophy in CMT2D mice. **a**–**d**, Histograms showing the axonal diameter frequencies in the sciatic nerves of 4-week-old wild-type (**a**), *Nrp1*$^{+/-}$ (**b**), *Gars*^{CMT2D} (CMT; **c**), and CMT;*Nrp1*$^{+/-}$ (**d**) mutant mice. $n = 3$ mice per group. Note the decreased numbers of larger-diameter axons in CMT;*Nrp1*$^{+/-}$ mutants compared with CMT, *Nrp1* heterozygous, and wild-type controls.

©2015 Macmillan Publishers Limited. All rights reserved

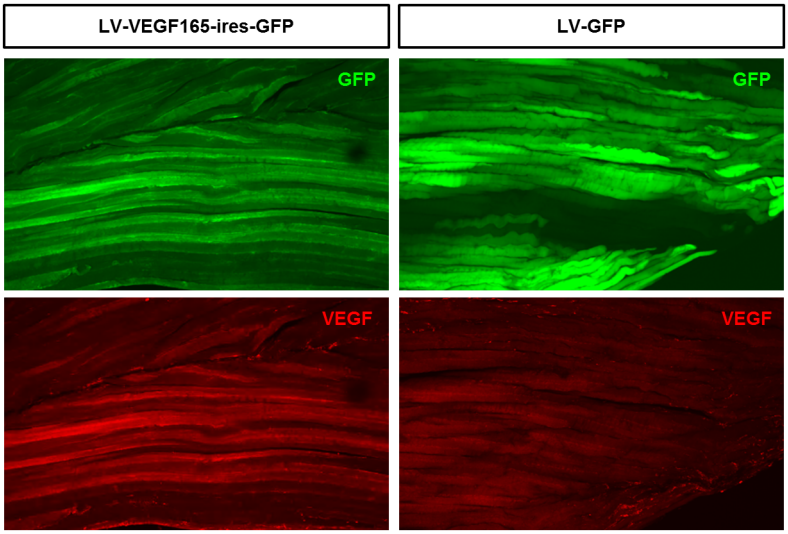

Extended Data Figure 8 | Expression level of VEGF in mouse muscles. The expression level of VEGF proteins in muscle fibres of mice injected with lentivirus expressing LV-VEGF$_{165}$-IRES-GFP versus LV-GFP was determined by immunostaining with anti-VEGF antibodies. Note that the expression level of VEGF in LV-VEGF-infected muscles is significantly higher than in LV-GFP-infected control groups.

©2015 Macmillan Publishers Limited. All rights reserved

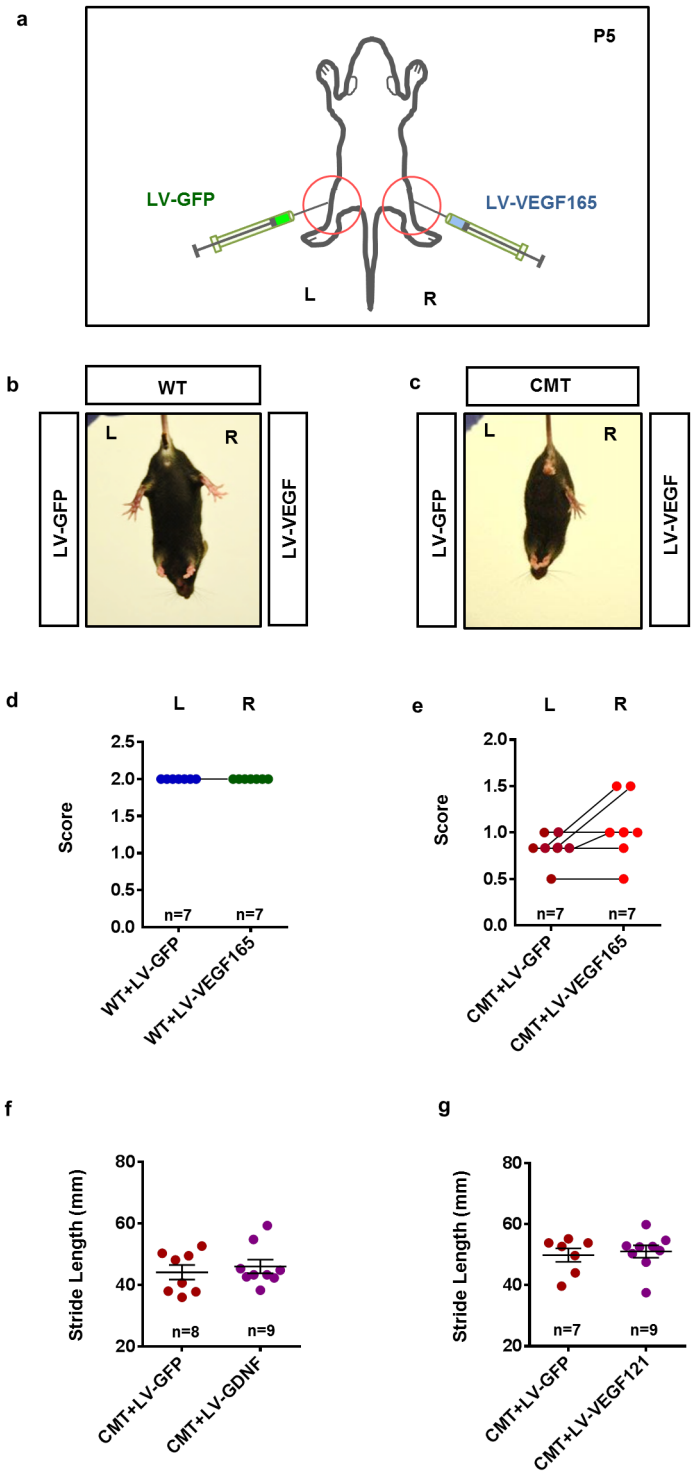

Extended Data Figure 9 | VEGF treatment retains limb strength in CMT2D mice. **a**, Diagram showing that lentiviral vectors encoding GFP (LV-GFP) or VEGF-A_{165} (LV-$VEGF_{165}$) are injected unilaterally into each hindlimb of the same $GlyRS^{CMT2D}$ mutant mouse at P5. **c**, **e**, At 5 weeks, LV-GFP-injected legs (L, left) of CMT2D animals have largely lost their ability to extend, while LV-VEGF165-treated legs (R, right) retained more limb strength with significantly higher scores in the hindlimb extension test (three out of seven animals). $P < 0.05$ (permutation test). **b**, **d**, No significant difference was observed between both injected legs of wild-type animals in the hindlimb extension test. **f**, **g**, GDNF and VEGF-A_{121} treatments fail to improve stride length in CMT2D mice. Walking strides of 2-month-old CMT2D mice bilaterally injected with lentiviral vectors (LV) encoding GFP, GDNF or VEGF-A_{121}. No significant difference of hindlimb stride length was observed between animals treated with LV-GDNF, LV-VEGF-A_{121}, and LV-GFP controls.

©2015 Macmillan Publishers Limited. All rights reserved

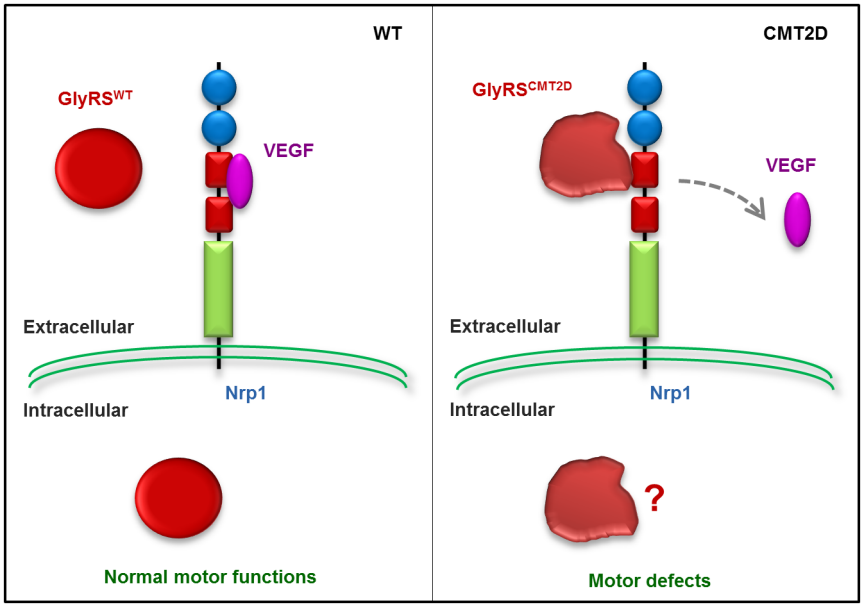

Extended Data Figure 10 | A simplified model for the neomorphic binding activity of GlyRS^{CMT2D}. Left, GlyRS^{WT} is a multifunctional protein with both intracellular and extracellular distributions. VEGF–Nrp1 signalling is an essential pathway for survival and function of motor neurons. (Note that VEGF may also act synergistically with other trophic factors, and/or maintain motor function indirectly by acting on Nrp1 receptors on non-motor neurons.) Right, CMT2D mutations alter the conformation of GlyRS, enabling GlyRS^{CMT2D} to bind Nrp1. This aberrant interaction antagonizes the binding of VEGF to Nrp1, contributing to motor defects in CMT2D. Our results do not exclude the possibility that GlyRS^{CMT2D} may also interact with other extracellular and/or intracellular targets, related to CMT2D pathology.

©2015 Macmillan Publishers Limited. All rights reserved